ACS APPLIED MATERIALS & INTERFACES

Research Article

www.acsami.org

Synthesis of Hierarchical Porous Carbon Monoliths with Incorporated Metal–Organic Frameworks for Enhancing Volumetric Based CO_2 Capture Capability

Dan Qian, Cheng Lei, Guang-Ping Hao, Wen-Cui Li, and An-Hui Lu*

State Key Laboratory of Fine Chemicals, School of Chemical Engineering, Faculty of Chemical, Environmental and Biological Science and Technology, Dalian University of Technology, Dalian 116024, P. R. China

ABSTRACT: This work aims to optimize the structural features of hierarchical porous carbon monolith (HCM) by incorporating the advantages of metal–organic frameworks (MOFs) ($Cu_3(BTC)_2$) to maximize the volumetric based CO_2 capture capability (CO_2 capacity in cm^3 per cm^3 adsorbent), which is seriously required for the practical application of CO_2 capture. The monolithic HCM was used as a matrix, in which $Cu_3(BTC)_2$ was in situ synthesized, to form HCM-$Cu_3(BTC)_2$ composites by a step-by-step impregnation and crystallization method. The resulted HCM-$Cu_3(BTC)_2$ composites, which retain the monolithic shape and exhibit unique hybrid structure features of both HCM and $Cu_3(BTC)_2$, show high CO_2 uptake of 22.7 cm^3 cm^{-3} on a volumetric basis. This value is nearly as twice as the uptake of original HCM. The dynamic gas separation measurement of HCM-$Cu_3(BTC)_2$, using 16% (v/v) CO_2 in N_2 as feedstock, illustrates that CO_2 can be easily separated from N_2 under the ambient conditions and achieves a high separation factor for CO_2 over N_2, ranging from 67 to 100, reflecting a strongly competitive CO_2 adsorption by the composite. A facile CO_2 release can be realized by purging an argon flow through the fixed-bed adsorber at 25 °C, indicating the good regeneration ability.

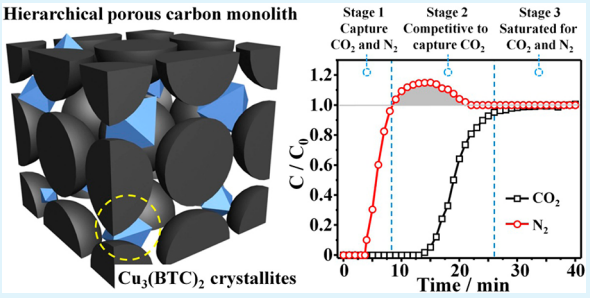

KEYWORDS: *hierarchical porous carbon monolith, MOFs, composites, CO_2 capture, volumetric based CO_2 capture capability, dynamic gas separation*

INTRODUCTION

Predictions of future climate change have triggered extensive research for ways to mitigate the emissions of "greenhouse" carbon dioxide (CO_2). Among the various technologies and processes that have been developed for the capture of CO_2,[1−4] sorption based separation using solid CO_2 sorbents such as zeolites,[5] monox,[6] porous carbon materials,[7−18] metal based adsorbents,[19−21] metal–organic frameworks (MOFs),[22−26] and microporous organic polymer (MOP)[27−29] have attracted much attention over several years. Each of those materials has its own advantages and disadvantages on CO_2 capture. This has been systematically discussed in the recent reviews.[1−4,30] It is thus highly desirable to develop novel adsorbent materials with combinational unique advantages of these materials and it would provide a significant advance in the application of CO_2 capture.

Porous carbon material is considered to be one of the most promising candidates for CO_2 capture due to its low cost, high thermal and chemical stability, excellent CO_2 adsorption capacity, and facile regeneration ability.[9] In the past few years, novel porous carbon materials such as carbide-derived carbons, carbon molecular sieves, N-doped porous carbons, and carbons that are prepared by template synthetic procedures or the physically and chemically activating method[7−18] have been investigated, and most of them show superior performance for CO_2 capture. In order to satisfy the requirement for practical application, the synthesis of self-supporting monolithic porous carbons is seriously desirable because monoliths can avoid excessive pressure drop in fixed-bed adsorber and dusting problems. Recently, we have demonstrated a facile and rapid method to prepare N-doped hierarchical porous carbon monoliths (HCMs), which show outstanding CO_2 capture capacity and facile regeneration ability at room temperature.[31,32] The obtained HCMs exhibit multilength scale porosity, i.e., macropores and micropores, which are responsible for facilitating gas diffusion and CO_2 adsorption, respectively. In addition, for the practical application, volumetric based CO_2 capture ability is seriously important because the volume of the fixed-bed adsorber is restricted. On the basis of this consideration, we had a design to optimize the structural features of HCM, aiming to maximize its volumetric based CO_2 capture capability.

Considering the fact that the self-supporting HCM has an abundance of micrometer sized macropores, which allows it to host foreign components, particularly those showing high CO_2 capture capability, the synthesis of HCM based composite may allow a further improvement on its volumetric based CO_2 capture ability, by optimizing its structure features. Nowadays,

Received: August 24, 2012
Accepted: October 16, 2012
Published: October 16, 2012

   dx.doi.org/10.1021/am301772k | *ACS Appl. Mater. Interfaces* 2012, 4, 6125–6132

another inexpensive material MOF, $Cu_3(BTC)_2$ introduced by Chui,[24] has drawn great attention due to its excellent ability to capture CO_2.[33,34] Conventionally, as-synthesized MOFs are obtained in the form of powder and thus limit their practical application. Although there are some reports on the preparation of MOFs composites[35−42] to achieve a macroscopic shape such as monolith or foam, the research of incorporating HCM with MOFs to enhance the volumetric based CO_2 capture capability of the original HCM has not been reported yet. In this study, we reported a new synthesis of such HCM-$Cu_3(BTC)_2$ composite and investigated its CO_2 adsorption properties in detail.

EXPERIMENTAL SECTION

Synthesis of Hierarchical Porous Carbon Monolith (HCM). The synthesis of HCM was according to our previous works.[31,32] HCM was synthesized by copolymerization of resorcinol and formaldehyde in the presence of methylimidazole (MIM) as the catalyst at ambient conditions. The polymer monolith was quickly formed within 15 min at the ambient temperature. In a typical synthesis, resorcinol (3.000 g) was dissolved in 16 mL of water to form a clear solution. Afterward, MIM (164 μL) and oleic acid (500 μL) were added into the solution in sequence. Subsequently, 4.420 g of formalin (37 wt %) containing formaldehyde was quickly injected into the solution during stirring. The white homogeneous emulsion was then sealed and transferred into an oven at 90 °C. The emulsion quickly turned yellow and solidified within 15 min to form a monolithic gel. This gel was cured for an additional 4 h. The resulting polymer monolith was dried at 50 °C for 24 h followed by pyrolysis at 800 °C for 2 h under the nitrogen atmosphere to obtain HCM.

Synthesis of HCM-$Cu_3(BTC)_2$ Composites. The synthesis of $Cu_3(BTC)_2$ was based on a procedure described elsewhere.[23] $Cu(NO_3)_2{\cdot}3H_2O$ (0.400 g) was stirred for 10 min in 10 mL of solvent consisting of dimethyl formamide (DMF), ethanol, and water (1:1:1, volume ratio) in a 15 mL flasket. Then, 1,3,5-benzenetricarboxylic acid (H_3BTC) (0.200 g) was added into the blue, clear solution, followed by continued stirring for 10 min to form MOF precursor solution. Then, the flasket was tightly capped and transferred into an oven at 90 °C for 20 h. The obtained blue crystals were washed with water and ethanol, followed by filtering and activating at 200 °C under the nitrogen atmosphere for 12 h to give dark blue powders.

HCM-$Cu_3(BTC)_2$ composites were synthesized by a step-by-step impregnation and crystallization method. First, the MOF precursor solution was obtained as indicated above. Then, the MOF precursor solution was carefully dropped onto the surface of HCM by a pipettor, and the solution was rapidly sucked by the HCM. The dropping continued until the MOF precursor solution was overflowed on the HCM surface. Afterward, the HCM was put into the MOF precursor solution to make sure the HCM was completely immerged. Then, the flasket was sealed and transferred into an oven at 90 °C for 20 h. The monolithic HCM-$Cu_3(BTC)_2$ was carefully separated from $Cu_3(BTC)_2$ powders and washed with water and ethanol. The obtained HCM-$Cu_3(BTC)_2$ was dried at 90 °C for 12 h and further activated at 200 °C for 6 h under the nitrogen atmosphere.

In order to increase the amount of $Cu_3(BTC)_2$ incorporated with HCM, the obtained HCM-$Cu_3(BTC)_2$ was repetitively impregnated by MOF precursor solution. The obtained composites were named as HCM-$Cu_3(BTC)_2$-x, where x means the number of impregnation steps.

Characterization. Nitrogen sorption experiments were carried out at 77 K using a Micromeritics TriStar 3000 instrument. All the samples were evacuated at 200 °C for 6 h prior to the measurements. The Brunauer−Emmett−Teller (BET) method was utilized to calculate the specific surface areas (S_{BET}). Micropore surface areas (S_{micro}) and micropore volumes (V_{micro}) were calculated by the t-plot method. Total pore volumes (V_{total}) were estimated from the amount adsorbed at P/P_0 = 0.99. Scanning electron microscope (SEM) investigations were carried out with a Hitachi S-4800 instrument. Powder X-ray diffraction (XRD) patterns were recorded on a D/Max-2400 diffract meter using a Cu Kα X-ray radiation, with a voltage of 45 kV and current of 40 mA. Fourier-transform infrared (FT-IR) spectra were recorded on a Nicolet 6700 instrument with the wave range of 500−4000 cm^{-1}. The thermal decomposition behaviors of the products were monitored using a simultaneous thermal analyzer (Netzsch STA 449 F3) from 40 to 600 °C under nitrogen atmosphere with a heating rate of 10 °C min^{-1}. Hg intrusion isotherms and pore size distributions (PSDs) of the pores larger than 50 nm were measured using a Micromeritics AutoPore IV 9500 analyzer.

CO_2 Adsorption Measurements. *Equilibrium Gas Adsorption Measurements.* The CO_2 adsorption isotherms were measured using a Micromeritics ASAP 2020 static volumetric analyzer at 25 °C. Prior to each adsorption experiment, the samples were degassed for 2 h at 200 °C to ensure that the residual pressure fell below 5×10^{-3} mbar. After the samples were cooled down to the room temperature, CO_2 was introduced into the system. The CO_2 adsorption capacity in terms of adsorbed volume under standard temperature and pressure (STP) were then recorded.

Dynamic Gas Separation Measurements. The separation measurements of CO_2 from CO_2/N_2 binary mixture were performed in a fixed-bed adsorber (a stainless steel tube with an inner diameter of 8 mm and a length of 130 mm) operated at ∼1 bar and 25 °C, which was controlled by the pressure controller and thermostatic water bath, respectively. The adsorbent was first heated to 95 °C in Ar with a flow rate of 50 mL min^{-1} for 2 h. Then, the breakthrough experiment was carried out by switching abruptly from Ar to the mixture gas containing 16% (v/v) of CO_2 in N_2 with a total flow rate of 7 mL min^{-1}. The effluent gas was monitored online using an Agilent 7890A gas chromatograph with a TCD detector.

RESULTS AND DISCUSSION

Structure and Unique Properties of HCM-$Cu_3(BTC)_2$ Composites. Scheme 1 illustrates the procedure for the preparation of HCM-$Cu_3(BTC)_2$ composites by the impregnation and crystallization method. In the procedure, we first used a pipettor to impregnate the HCM by MOF precursor solution before the HCM was entirely dipped into MOF precursor solution, to ensure the μm-size macropores of HCM were fully impregnated by MOF precursor solution. Otherwise, if the HCM was directly dipped into the MOF precursor solution, the gas inside the HCM could hardly be released from the pores and it would further restrain the diffusion of MOF precursor solution into the μm-size macropores of HCM. Thus, the step of preimpregnating the HCM by MOF precursor solution before the growth of $Cu_3(BTC)_2$ crystallites[43−45] inside the HCM matrix is indispensible. Before analyses, the obtained HCM-$Cu_3(BTC)_2$ composites were intensively washed with water and ethanol to remove all the remaining solvable compounds.

Scheme 1. Procedure to Fabricate HCM-$Cu_3(BTC)_2$-x

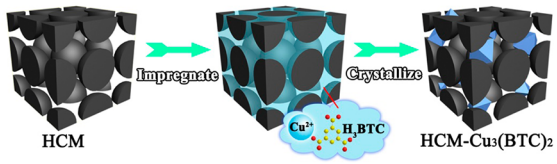

The mesoscopic structure of the HCM-$Cu_3(BTC)_2$ composites and the parent materials (HCM and $Cu_3(BTC)_2$) were characterized by SEM. Figure 1a shows that HCM exhibits fully interconnected macropores and a sponge-like branched skeleton. Figure 1b shows that $Cu_3(BTC)_2$ crystallites exhibit the octahedral geometry and the crystallites size varies between

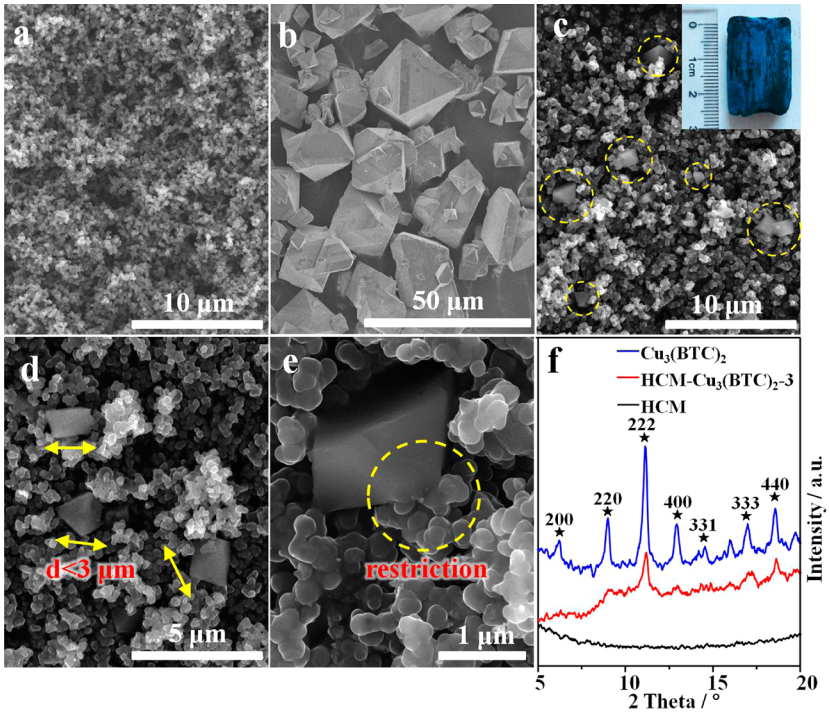

Figure 1. SEM micrographs of HCM (a), $Cu_3(BTC)_2$ (b), and HCM-$Cu_3(BTC)_2$-3 (c, d, e). (f) XRD patterns of HCM, $Cu_3(BTC)_2$, and HCM-$Cu_3(BTC)_2$-3.

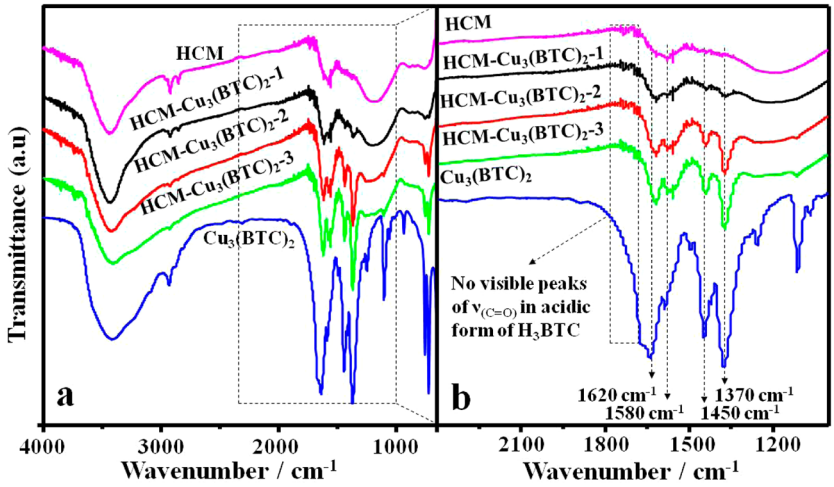

Figure 2. (a) Infrared spectra of HCM, $Cu_3(BTC)_2$, and HCM-$Cu_3(BTC)_2$-x over the wavenumber range of 500−4000 cm^{-1} and (b) the detailed wavenumber range of 1000−2400 cm^{-1}.

2 and 30 μm. In a comparison of the crystallites size of $Cu_3(BTC)_2$ and the macropore size of HCM, the macropores of HCM provide a microenvironment for the growth of $Cu_3(BTC)_2$ crystallites. Indeed, the SEM micrograph (Figure 1c) clearly displays that $Cu_3(BTC)_2$ crystallites are born within the macropores of the HCM matrix. The sponge-like skeleton of HCM before and after MOF growth remains unchanged. The octahedral $Cu_3(BTC)_2$ crystallites are well dispersed within the HCM matrix. The photograph (Figure 1c, inset) shows that HCM can retain its monolithic shape after impregnation and a crystal growth process, indicating good structure stability. As seen in Figure 1d, the sizes of the $Cu_3(BTC)_2$ crystallites are generally less than 3 μm, which are smaller than that of the $Cu_3(BTC)_2$ growing freely. Moreover, the SEM image in Figure 1e shows that the carbon skeletons are in close contact with the surface of $Cu_3(BTC)_2$ crystallites. This suggests that the carbon skeleton played a restriction effect on the growth of $Cu_3(BTC)_2$ crystallites, and thus, the crystallite sizes were matched well with the macropores of the HCM matrix.

Figure 1f presents the XRD patterns of the synthesized HCM, $Cu_3(BTC)_2$, and HCM-$Cu_3(BTC)_2$-3. The results show that no visible reflections of HCM were detected, while $Cu_3(BTC)_2$ sample shows clear reflections in the 2θ range of 5−20°, which can be assigned as (200), (220), (222), (400), (331), (333), and (440) of the octahedral geometry of $Cu_3(BTC)_2$. This result is in good agreement with the previous reports.[38,39] Due to the presence of amorphous carbon matrix, the XRD pattern of the HCM-$Cu_3(BTC)_2$-3 composite displays certain weakening of the diffraction intensity, while the

dx.doi.org/10.1021/am301772k | ACS Appl. Mater. Interfaces 2012, 4, 6125−6132

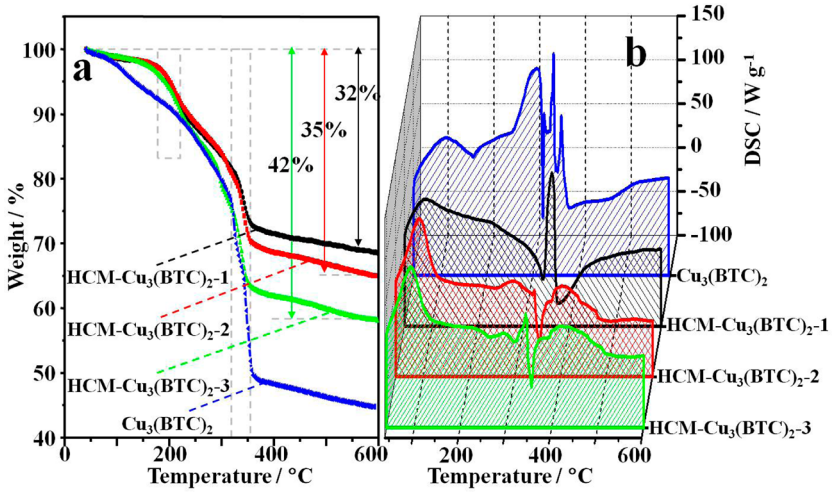

Figure 3. TGA (a) and DSC (b) curves of pure $Cu_3(BTC)_2$ and HCM-$Cu_3(BTC)_2$ composites.

Table 1. Textural Parameters and CO_2 Adsorption Capacity at Room Temperature and Atmospheric Pressure of HCM, $Cu_3(BTC)_2$, and Their Composites

					CO_2 uptake	
samples	S_{BET} (m^2/g)	V_{total} (cm^3/g)	V_{micro} (cm^3/g)	bulk density[a] (g/cm)	(cm^3/cm)	(mmol/g)
HCM	668	0.39	0.27	0.22	12.9	2.61
$Cu_3(BTC)_2$	1448	0.70	0.57	–[b]	46.4	3.98
HCM-$Cu_3(BTC)_2$-1	270	0.18	0.10	0.26	13.8	2.36
HCM-$Cu_3(BTC)_2$-2	455	0.23	0.18	0.31	16.6	2.37
HCM-$Cu_3(BTC)_2$-3	516	0.26	0.20	0.37	22.7	2.75

[a]The bulk volume was calculated by measuring the diameter and length of the columnar HCM. [b]The packing density and crystal density of $Cu_3(BTC)_2$ are 0.88 g cm^{-3} and 0.52 g cm^{-3}, respectively, which are taken from ref 49. The volume based CO_2 uptake of $Cu_3(BTC)_2$ is according to its packing density.

reflection peaks (220), (222), (400), (333), and (440) match well with the crystal faces of pure $Cu_3(BTC)_2$. Considering the results supported by SEM and XRD, one can conclude that the monolithic composite consisting of self-supporting carbon matrix and $Cu_3(BTC)_2$ crystallites has been successfully synthesized. It has the configuration of micrometer-sized $Cu_3(BTC)_2$ crystallites immobilized within the macropores of HCM.

The parent materials ($Cu_3(BTC)_2$ and HCM) and HCM-$Cu_3(BTC)_2$-*x* were characterized by FT-IR spectroscopy (Figure 2). It should be noted that, for carbon material HCM, the highly developed porosity strongly adsorbs the IR radiation, and thus, only the signals of the relative abundant functionalities are observed. A comparison of HCM and $Cu_3(BTC)_2$ reveals that the bands in the range of 1620−1580 cm^{-1} and 1500−1400 cm^{-1} can be assigned to the carbon−carbon stretchings in the aromatic ring, and the out of plane C−H bending modes are clearly visible at around 700 cm^{-1}. The bands at ∼1580, ∼1450, and ∼1370 cm^{-1} stand for bridging bidentate coordination of carboxylate group, indicating that the synthesized composite was incorporated with MOFs. Besides, no visible peak in the range of 1680−1750 cm^{-1} is observed, excluding the presence of the acidic form of H_3BTC.[46−48] The progressive increase in the intensity of the bands can be noticed as the content in $Cu_3(BTC)_2$ increases, indicating that the synthesized composites were incorporated with MOFs.

To examine the thermal stability of the as-made HCM-$Cu_3(BTC)_2$ composites, thermogravimetric analyses were carried out under a nitrogen atmosphere with a heating rate of 10 °C min^{-1} and the results were shown in Figure 3. The thermogravimetric analysis (TGA) results (Figure 3a) reveal that all HCM-$Cu_3(BTC)_2$ composites have a ∼10% weight loss below 200 °C, which can be attributed to the departure of solvent molecules mainly including DMF. On the basis of this result, we activated the HCM-$Cu_3(BTC)_2$ composites at 200 °C for 6 h under a N_2 atmosphere in order to empty organic molecules trapped in the micropores after they were dried at 90 °C. The thermogravimetric (TG) curves of the HCM-$Cu_3(BTC)_2$ composites show similar thermal behavior as $Cu_3(BTC)_2$ but with a slightly delayed weight loss before 180 °C. This is due to the encapsulation and protection effect of the carbon matrix. When the temperature reaches higher than 300 °C, HCM-$Cu_3(BTC)_2$ composites display a sharp weight loss in TGA curves and intense endothermic−exothermal peaks in DSC curves, which are familiar with the pure $Cu_3(BTC)_2$ in the temperature range of 325−350 °C (Figure 3b) due to the decomposition of $Cu_3(BTC)_2$ crystallites.[23,24] Hence, TG analyses, on the other hand, further confirm that $Cu_3(BTC)_2$ was successfully incorporated with HCM to form HCM-$Cu_3(BTC)_2$ composites. When the temperatures exceed 400 °C, the HCM-$Cu_3(BTC)_2$ composites show slight weight loss, owing to the stability of HCM and the carbonization of $Cu_3(BTC)_2$.

At 600 °C, the weight losses of HCM-$Cu_3(BTC)_2$-1, HCM-$Cu_3(BTC)_2$-2, and HCM-$Cu_3(BTC)_2$-3 are 35%, 38%, and 42% respectively. The weight losses provide evidence of different amounts of $Cu_3(BTC)_2$ crystallites incorporated with HCM.

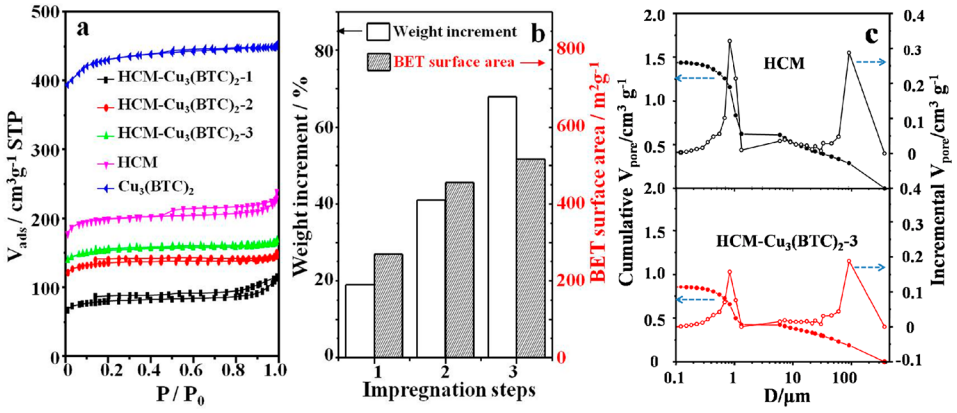

Figure 4. (a) Nitrogen sorption isotherms at 77 K. (b) Weight increments and BET surface areas of HCM-$Cu_3(BTC)_2$-*x* composites vs the number of impregnation steps. (c) Hg intrusion curves and differential PSDs of HCM and HCM-$Cu_3(BTC)_2$-3.

The weight increments of HCM-$Cu_3(BTC)_2$ composites were calculated using the following formula:

$$\text{weight increment} = [W_{\text{HCM-Cu}_3(\text{BTC})_2} - W_{\text{HCM}}]/W_{\text{HCM}}$$

The calculated weight increments of HCM-$Cu_3(BTC)_2$-1, HCM-$Cu_3(BTC)_2$-2, and HCM-$Cu_3(BTC)_2$-3 are 19%, 41%, and 68%, respectively. These results show that the composites had a regular weight increment of approximately 20% through each impregnation step. Furthermore, the previously grown $Cu_3(BTC)_2$ crystallites in HCM would accelerate the successive growth of fresh $Cu_3(BTC)_2$ analogues for the next impregnation step.[45] It leads to an approximately 27% weight increment after the third impregnation.

According to the bulk density of HCM and crystal density of $Cu_3(BTC)_2$ (Table 1), about a 17% volume fraction of HCM was occupied by $Cu_3(BTC)_2$ crystallites for HCM-$Cu_3(BTC)_2$-3. As supported by the photograph and SEM results of HCM-$Cu_3(BTC)_2$-3, a further impregnation step would lead to the formation of crystals outside the monolith, resulting in lower impregnation efficiency. In addition, considering the gas diffusivity in the monolithic HCM and timesaving procedure, no further impregnation steps were carried out.

The porous structure of all the samples was analyzed by N_2 sorption at 77 K. Porous parameters of the composites calculated from N_2 sorption isotherms are listed in Table 1. As shown in Figure 4a, the N_2 sorption isotherm of HCM is of type IV with a small hysteresis loop, indicating the combination of mesoporosity and microporosity. HCM has a surface area of 668 $m^2\ g^{-1}$ and a total pore volume of 0.39 $cm^3\ g^{-1}$. If HCM and $Cu_3(BTC)_2$ can retain their structure and porosity during the synthesis process, one can envisage an anticipative result of the composite, i.e., the N_2 uptake of HCM-$Cu_3(BTC)_2$-1 should be higher than that of the original HCM but lower than $Cu_3(BTC)_2$. However, the resultant HCM-$Cu_3(BTC)_2$-1 exhibits lower N_2 uptake than both original HCM and $Cu_3(BTC)_2$. This may be due to the serious microporosity and mesoporosity blockage of HCM by $Cu_3(BTC)_2$ precursor or nuclei at the initial stage, leading to the inferior textural parameters. A similar phenomenon has been observed that the surface areas of porous carbons after being modified with organic functional groups decreased significantly.[36,37,41,50−54] After three impregnation and crystallization steps, a sufficient amount of $Cu_3(BTC)_2$ crystallites were formed within the macropores of HCM. Under this condition, the contribution to the porosity by $Cu_3(BTC)_2$ partly compensates for that arising from the pore blockage of HCM. Figure 4b shows the variation of the BET surface areas of HCM-$Cu_3(BTC)_2$ composites vs the number of impregnation steps. By combining the results from TGA, one can conclude that high loading of $Cu_3(BTC)_2$ crystallites in HCM can enhance the N_2 uptake by showing higher BET surface areas. However, the porous parameters of the composite are still inferior to that of the original HCM. The presence of the macroporosity in HCM and HCM-$Cu_3(BTC)_2$-3 was confirmed by Hg intrusion analysis. As shown in Figure 4c, the curves of cumulative pore volume vs pore diameter show a continuous increase in mercury uptake with a decrease in pore diameter (i.e., increase of Hg intrusion pressure). Essentially, the curves of samples HCM and HCM-$Cu_3(BTC)_2$-3 are similar in shape, and the macropore sizes of these two samples are all concentrated at ∼0.85 μm. However, a significant difference is that the pore volume of HCM-$Cu_3(BTC)_2$-3 is lower than HCM, indicating that $Cu_3(BTC)_2$ crystals indeed have been formed within the macropores.

CO_2 Adsorption Performance of HCM-$Cu_3(BTC)_2$ Composites. The CO_2 molecule has a large electric quadrupole moment that arises from the strong dipole moments of the C═O bonds. The polarizability and the kinetic diameter of CO_2 are 29.11 × 10^{-25} cm^3 and 3.3 Å, respectively.[32] The nitrogen-doped monolithic HCM possesses intrinsic properties such as polar surface and abundant micropores; these features allow HCM to be an excellent CO_2 adsorbent, while a practical application requires that adsorbent has high adsorption CO_2 capacity per unit volume of adsorbent,[55] which highly depends on the bulk density of a synthesized material. To meet this demand, $Cu_3(BTC)_2$ crystallites were incorporated into the macropores of HCM, thus improving the volumetric based CO_2 capture capacity of HCM. This would enhance the competitive power of the HCM-$Cu_3(BTC)_2$ composites for practical CO_2 capture applications.

SEM and XRD results supported that μm-sized $Cu_3(BTC)_2$ crystallites were successfully incorporated within the macropores of the HCM matrix. Hence, though the weight of HCM-$Cu_3(BTC)_2$ composites increased with repeated impregnation steps, the bulky volume of the composites remain almost identical. The measured bulk densities of HCM, HCM-$Cu_3(BTC)_2$-1, HCM-$Cu_3(BTC)_2$-2, and HCM-$Cu_3(BTC)_2$-3 are 0.22, 0.26, 0.31, and 0.37 g cm^{-3}, respectively. The equilibrium CO_2 adsorption measurements were carried out at 25 °C, and the results (Figure 5a) reveal that HCM-

dx.doi.org/10.1021/am301772k | ACS Appl. Mater. Interfaces 2012, 4, 6125−6132

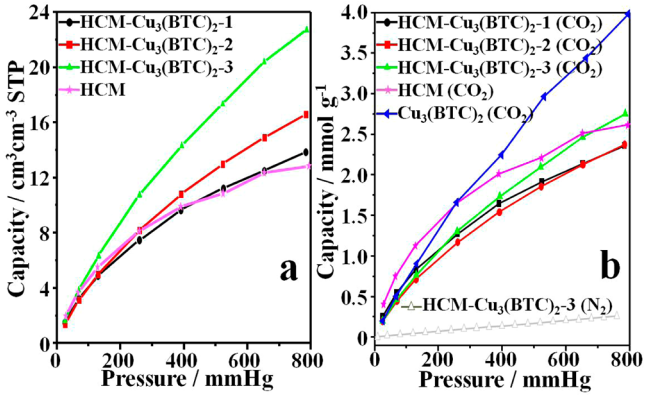

Figure 5. (a) CO_2 adsorption isotherms on a volumetric basis. (b) CO_2 and N_2 adsorption isotherms on a gravimetric basis.

$Cu_3(BTC)_2$ composites exhibit an obvious increment in CO_2 adsorption capacity on a volumetric basis compared with the original HCM. The HCM-$Cu_3(BTC)_2$-3 composite with the highest $Cu_3(BTC)_2$ loading can achieve maximum CO_2 uptake of 22.7 cm^3 STP per cm^3 at ~1 bar, which is almost as twice as the uptake of HCM (12.9 cm^3 STP per cm^3) under the same conditions. This result encourages a new principle on a rational design of CO_2 capture material by maximizing the capacity on a volumetric basis.

Figure 5b shows the gravimetric based CO_2 capture ability of all the samples. At low CO_2 partial pressures (<200 mmHg), HCM adsorbs more CO_2 molecules than $Cu_3(BTC)_2$ at a specific pressure; this is because HCM owns a large number of macropores, which facilitate CO_2 molecule diffusion throughout the monolith. While at relatively high CO_2 partial pressures (>400 mmHg), the increased concentration of CO_2 results in enhanced diffusion rate, so the micropore enriched $Cu_3(BTC)_2$ can capture more CO_2 molecules than HCM. Such different CO_2 adsorption behaviors and adsorption capacities of HCM and $Cu_3(BTC)_2$ finally influence CO_2 adsorption performance of HCM-$Cu_3(BTC)_2$ composites. HCM-$Cu_3(BTC)_2$-3, with a high loading of $Cu_3(BTC)_2$ crystallites, shows a similar adsorption isotherm as $Cu_3(BTC)_2$ and exhibits the largest CO_2 adsorption capacity compared to other composites. On the basis of the above-mentioned results, we preassembly deduce that HCM plays a major role in CO_2 adsorption at lower relative pressures, whereas $Cu_3(BTC)_2$ is at relatively higher pressures. The obtained HCM-$Cu_3(BTC)_2$-1 and HCM-$Cu_3(BTC)_2$-2 show slightly lower CO_2 adsorption capacity than that of HCM at ~1 bar due to the inferior porous structure. While thanks to the contribution to the porosity by $Cu_3(BTC)_2$, HCM-$Cu_3(BTC)_2$-3 shows the CO_2 uptake of 2.75 mmol g^{-1}, which surpasses the original HCM. The aforementioned results indicate that the HCM-$Cu_3(BTC)_2$-3 composite performs the best among the synthesized materials so far in this study. Subsequently, we focused on the investigation of the adsorption and separation properties of HCM-$Cu_3(BTC)_2$-3. The measured N_2 uptake of HCM-$Cu_3(BTC)_2$-3 was only 0.26 mmol g^{-1} at 25 °C (~1 bar), and the adsorption selectivity estimated from the ratio of the initial slopes of the CO_2 and N_2 adsorption isotherms is about 18.4,[56,57] while the selectivity estimated from the ratio of the amounts of CO_2 and N_2 adsorbed at ambient pressure is about 10.6.[58]

We also calculated the isosteric heat of adsorption (Q_{st}) of HCM-$Cu_3(BTC)_2$-3 (Figure 6) by fitting the CO_2 adsorption

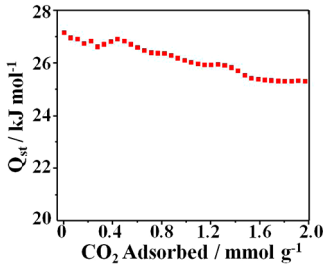

Figure 6. Isosteric heat of adsorption of HCM-$Cu_3(BTC)_2$-3 for CO_2 at different CO_2 loadings.

isotherms measured at 0 and 25 °C and applying a variant of the Clausius–Clapeyron equation.[57] Its Q_{st} lies in the range of 25.0–27.2 kJ mol^{-1}. The higher Q_{st} at the initial stage leads to a preferential adsorption of CO_2 over N_2. This can be explained by the strong quadrupolar interactions of CO_2 molecules with the heterogeneous pore walls (e.g., nitrogen-groups) at low pressures.

In order to evaluate the practical application of HCM-$Cu_3(BTC)_2$ for separation of CO_2 and N_2, we conducted dynamic breakthrough separation experiments[32,33,59] for HCM-$Cu_3(BTC)_2$-3 composite. A mixture stream of 16% (v/v) CO_2 balanced with N_2 was used as the feed gas, which approximately simulates a flue gas. Then, 1.034 g of HCM-$Cu_3(BTC)_2$-3 was filled into the column with a length of 130 mm and an internal diameter of 8 mm. The measured breakthrough curve (Figure 7a) can be divided into three stages. In stage 1 (0–8 min), both

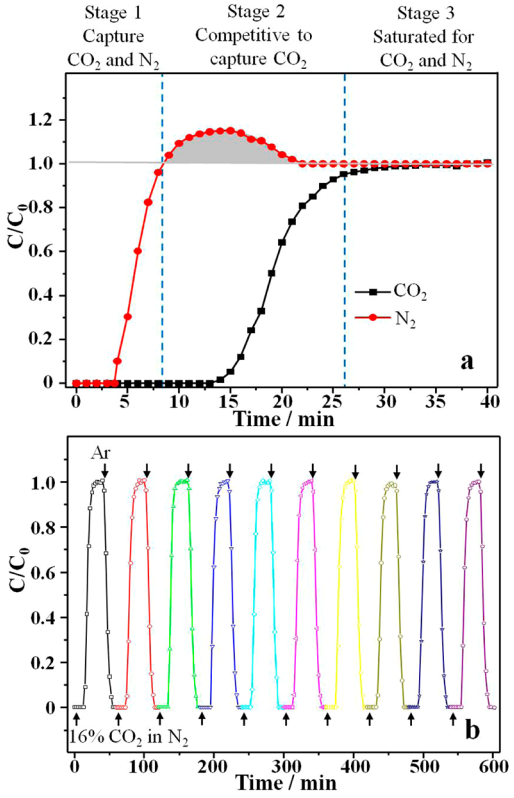

Figure 7. (a) Breakthrough curve of HCM-$Cu_3(BTC)_2$-3 using a stream of 16% (v/v) CO_2 in N_2 at 25 °C. (b) Recycle runs of CO_2 adsorption–desorption on HCM-$Cu_3(BTC)_2$-3 at 25 °C, using a stream of 16% (v/v) CO_2 in N_2, followed a regeneration by argon flow.

dx.doi.org/10.1021/am301772k | ACS Appl. Mater. Interfaces 2012, 4, 6125–6132

CO_2 and N_2 were captured because the adsorbent was not saturated with CO_2 and N_2. In stage 2 (8−26 min), CO_2 was continuingly captured by the adsorbent whereas no more N_2 was captured because the adsorbent was saturated with N_2. In addition, as the adsorbent was competitively/preferentially to capture CO_2, parts of the preadsorbed N_2 molecules were again expelled into the effluent stream by CO_2 molecules. This is why extra N_2 stream was observed in effluent stream. This phenomenon strongly evidenced that HCM-$Cu_3(BTC)_2$ composite can selectively capture CO_2 from N_2. In stage 3 (>26 min), the adsorbent was saturated with both CO_2 and N_2, so the flow rate and composition of the effluent stream were the same as the feed gas.

According to the breakthrough curve, we calculated CO_2 mass uptake capacity of HCM-$Cu_3(BTC)_2$-3 as 0.76 mmol g^{-1}, which coincides with the single component CO_2 adsorption datum (0.73 mmol g^{-1}) at the CO_2 partial pressure of 121 mmHg. While the N_2 mass uptake capacity is only 0.05 ± 0.01 mmol g^{-1}, which is much lower than the single component N_2 adsorption datum because of the competitive capture for CO_2, the calculated separation factor $S_{CO2/N2}$ for CO_2 over N_2 is estimated to be 67−100. The separation factors $S_{CO2/N2}$ is calculated as

$$S_{CO_2/N_2} = [q_{CO_2}/y_{CO_2}]/[q_{N_2}/y_{N_2}]$$

Herein, q_{CO2} and q_{N2} are the adsorbed amounts of CO_2 and N_2, respectively. y_{CO2} and y_{N2} are the mole fraction of CO_2 and N_2 in the gas phase.

The gas cycling experiment was carried out to verify the selective and reversible CO_2 capture capacity of the HCM-$Cu_3(BTC)_2$-3 composite (Figure 7b). The CO_2 saturated composite was subjected to an argon purge flow of 15 mL min^{-1} at 25 °C. After approximately 20 min, no CO_2 was detected in the effluent stream. Successive regeneration experiments show that HCM-$Cu_3(BTC)_2$-3 composite retains 92−96% of its intrinsic capture capacity after mild regeneration. Further, the cycling experiment does not lead to visible reduction of the capture capacity. The results signify that such HCM-$Cu_3(BTC)_2$ composite provides a high-capacity separation under very mild conditions for regeneration. High CO_2 capture capacity and separation selectivity, easy handling, and facile regeneration ability are desirable and indispensable properties for practical CO_2 capture applications. Hence, the dynamic results also confirm that the HCM-$Cu_3(BTC)_2$ composite is extremely selective for adsorbing CO_2 over N_2 and represents a major advance in CO_2 separation capacity.

CONCLUSIONS

To improve the volumetric based CO_2 adsorption capacity of a porous carbon material, we have successfully synthesized HCM with incorporated MOFs by an in situ crystal growth in a macropore environment through a repeat impregnation and crystallization strategy, leading to the formation of a composite with increased bulk density. To our knowledge, this is the first report on the preparation of HCM with incorporated MOF crystallites in situ grown within its free macropores. Such a unique feature allows an effective creation of a composite material by uniting those two particular solids. The resultant HCM-$Cu_3(BTC)_2$-3 exhibits high CO_2 uptake of 22.7 cm^3 cm^{-3} on a volumetric basis, which is twice the uptake of original HCM. Its dynamic capacity of CO_2 is 0.76 mmol g^{-1} at 25 °C, using 16% (v/v) CO_2 in N_2 as feedstock. A high separation factor of 67−100 for the capture of CO_2 over N_2 is achieved, indicating a strongly competitive CO_2 adsorption by the composite. Meanwhile, it undergoes a facile CO_2 release in argon at 25 °C, indicating a good regeneration capability. We believe that this study provides a new pathway of ingenious synthesis of monolithic porous carbon based composite materials by integration of the advantages of each starting material. The current synthesis may have an impact on the advance of new types of composite materials for practical application of CO_2 capture.

AUTHOR INFORMATION

Corresponding Author

*Fax/Tel: (+86)-411-84986112. E-mail: anhuilu@dlut.edu.cn.

Notes

The authors declare no competing financial interest.

ACKNOWLEDGMENTS

The project was supported by the Fundamental Research Funds for the Central Universities (DUT11ZD106), the Program for New Century Excellent Talents in University of China (NCET-09-0254), the Scientific Research Foundation for the Returned Overseas Chinese Scholars, State Education Ministry, and the Ph.D. Programs Foundation (20100041110017) of Ministry of Education of China.

REFERENCES

(1) Rochelle, G. T. *Science* **2009**, *325*, 1652−1654.
(2) D'Alessandro, D. M.; Smit, B.; Long, J. R. *Angew. Chem., Int. Ed.* **2010**, *49*, 6058−6082.
(3) Choi, S.; Drese, J. H.; Jones, C. W. *ChemSusChem* **2009**, *2*, 796−854.
(4) Hedin, N.; Chen, L. J.; Laaksonen, A. *Nanoscale* **2010**, *2*, 1819−1841.
(5) Siriwardane, R. V.; Shen, M.-S.; Fisher, E. P. *Energy Fuels* **2005**, *19*, 1153−1159.
(6) Hicks, J. C.; Drese, J. H.; Fauth, D. J.; Gray, M. L.; Qi, G.; Jones, C. W. *J. Am. Chem. Soc.* **2008**, *130*, 2902−2903.
(7) Drage, T. C.; Blackman, J. M.; Pevida, C.; Snape, C. E. *Energy Fuels* **2009**, *23*, 2790−2796.
(8) Radosz, M.; Hu, X.; Krutkramelis, K.; Shen, Y. *Ind. Eng. Chem. Res.* **2008**, *47*, 3783−3794.
(9) Sevilla, M.; Valle-Vigón, P.; Fuertes, A. B. *Adv. Funct. Mater.* **2011**, *21*, 2781−2787.
(10) Xia, Y. D.; Mokaya, R.; Walker, G. S.; Zhu, Y. Q. *Adv. Energy Mater.* **2011**, *1*, 678−683.
(11) Zhao, L.; Bacsik, Z.; Hedin, N.; Wei, W.; Sun, Y.; Antonietti, M.; Titirici, M.-M. *ChemSusChem* **2010**, *3*, 840−845.
(12) Gutiérrez, M. C.; Carriazo, D.; Ania, C. O.; Parra, J. B.; Ferrer, M. L.; Monte, F. D. *Energy Environ. Sci.* **2011**, *4*, 3535−3544.
(13) Hu, X.; Radosz, M.; Cychosz, K. A.; Thommes, M. *Environ. Sci. Technol.* **2011**, *45*, 7068−7074.
(14) Liang, C. D.; Li, Z. J.; Dai, S. *Angew. Chem., Int. Ed.* **2008**, *47*, 3696−3717.
(15) Stein, A.; Wang, Z.; Fierke, M. A. *Adv. Mater.* **2009**, *21*, 265−293.
(16) Li, Q.; Yang, J. P.; Feng, D.; Wu, Z. X.; Wu, Q. L.; Park, S. S.; Ha, C.-S.; Zhao, D. Y. *Nano Res.* **2010**, *3*, 632−642.
(17) Pevida, C.; Drage, T. C.; Snape, C. E. *Carbon* **2008**, *46*, 1464−1474.
(18) Pevida, C.; Plaza, M. G.; Arias, B.; Fermoso, J.; Rubiera, F.; Pis, J. J. *Appl. Surf. Sci.* **2008**, *254*, 7165−7172.
(19) Ochoa-Fernández, E.; Rønning, M.; Grande, T.; Chen, D. *Chem. Mater.* **2006**, *18*, 6037−6046.
(20) Lee, S. C.; Chae, H. J.; Lee, S. J.; Choi, B. Y.; Yi, C. K.; Lee, J. B.; Ryu, C. K.; Kim, J. C. *Environ. Sci. Technol.* **2008**, *42*, 2736−2741.

(21) Ochoa-Fernández, E.; Rønning, M.; Yu, X.; Grande, T.; Chen, D. *Ind. Eng. Chem. Res.* **2008**, *47*, 434−442.
(22) Furukawa, H.; Ko, N.; Go, Y. B.; Aratani, N.; Choi, S. B.; Choi, E.; Yazaydin, A. Ö.; Snurr, R. Q.; O'Keeffe, M.; Kim, J.; Yaghi, O. M. *Science* **2010**, *329*, 424−428.
(23) Millward., A. R.; Yaghi, O. M. *J. Am. Chem. Soc.* **2005**, *127*, 17998−17999.
(24) Chui, S. S.-Y.; Lo, S. M.-F.; Charmant, J. P. H.; Orpen, A. G.; Williams, I. D. *Science* **1999**, *283*, 1148−1150.
(25) Furukawa, H.; Yaghi, O. M. *J. Am. Chem. Soc.* **2009**, *131*, 8875−8883.
(26) Choi, Y. J.; Choi, J. H.; Choi, K. M.; Kang, J. K. J. *Mater. Chem.* **2011**, *21*, 1073−1078.
(27) Farha, O. K.; Spokoyny, A. M.; Hauser, B. G.; Bae, Y.-S.; Brown, S. E.; Snurr, R. Q.; Mirkin, C. A.; Hupp, J. T. *Chem. Mater.* **2009**, *21*, 3033−3035.
(28) Farha, O. K.; Bae, Y.-S.; Hauser, B. G.; Spokoyny, A. M.; Snurr, R. Q.; Mirkin, C. A.; Hupp, J. T. *Chem. Commun.* **2010**, *46*, 1056−1058.
(29) McKeown, N. B.; Budd, P. M. *Macromolecules* **2010**, *43*, 5163−5176.
(30) Hao, G.-P.; Li, W.-C.; Lu, A.-H. *J. Mater. Chem.* **2011**, *21*, 6447−6451.
(31) Hao, G.-P.; Li, W.-C.; Qian, D.; Lu, A.-H. *Adv. Mater.* **2010**, *22*, 853−857.
(32) Hao, G.-P.; Li, W.-C.; Qian, D.; Wang, G.-H.; Zhang, W.-P.; Zhang, T.; Wang, A.-Q.; Schüth, F.; Bongard, H.-J.; Lu, A.-H. *J. Am. Chem. Soc.* **2011**, *133*, 11378−11388.
(33) Hamon, L.; Jolimaître, E.; Pirngruber, G. D. *Ind. Eng. Chem. Res.* **2010**, *49*, 7497−7503.
(34) Yazaydın, A. Ö.; Benin, A. I.; Faheem, S. A.; Jakubczak, P.; Low, J. J.; Willis, R. R.; Snurr, R. Q. *Chem. Mater.* **2009**, *21*, 1425−1430.
(35) Küsgens, P.; Siegle, S.; Kaskel, S. *Adv. Eng. Mater.* **2009**, *11*, 93−95.
(36) Schwab, M. G.; Senkovska, I.; Rose, M.; Koch, M.; Pahnke, J.; Jonschker, G.; Kaskel, S. *Adv. Eng. Mater.* **2008**, *10*, 1151−1155.
(37) Górka, J.; Fulvio, P. F.; Pikus, S.; Jaroniec, M. *Chem. Commun.* **2010**, *46*, 6798−6800.
(38) Biemmi, E.; Scherb, C.; Bein, T. *J. Am. Chem. Soc.* **2007**, *129*, 8054−8055.
(39) Shekhah, O.; Wang, H.; Kowarik, S.; Schreiber, F.; Paulus, M.; Tolan, M.; Sternemann, C.; Evers, F.; Zacher, D.; Fischer, R. A.; Wöll, C. *J. Am. Chem. Soc.* **2007**, *129*, 15118−15119.
(40) Nan, J. P.; Dong, X. L.; Wang, W. J.; Jin, W. Q.; Xu, N. P. *Langmuir* **2011**, *27*, 4309−4312.
(41) Petit, C.; Bandosz, T. J. *Adv. Mater.* **2009**, *21*, 4753−4757.
(42) Petit, C.; Bandosz, T. J. *Adv. Funct. Mater.* **2010**, *20*, 111−118.
(43) Biemmi, E.; Christian, S.; Stock, N.; Bein, T. *Microporous Mesoporous Mater.* **2009**, *117*, 111−117.
(44) Seo, Y.-K.; Hundal, G.; Jang, I. T.; Hwang, Y. K.; Jun, C.-H.; Chang, J.-S. *Microporous Mesoporous Mater.* **2009**, *119*, 331−337.
(45) Khan, N. A.; Haque, E.; Jhung, S. H. *Phys. Chem. Chem. Phys.* **2010**, *12*, 2625−2631.
(46) Petit, C.; Mendoza, B.; Bandosz, T. J. *Langmuir* **2010**, *26*, 15302−15309.
(47) Shi, N.; Yin, G.; Han, M.; Jiang, L.; Xu, Z. *Chem.—Eur. J.* **2008**, *14*, 6255−6259.
(48) Petit, C.; Burress, J.; Bandosz, T. J. *Carbon* **2011**, *49*, 563−572.
(49) Senkovska, I.; Kaskel, S. *Microporous Mesoporous Mater.* **2008**, *112*, 108−115.
(50) O'Neill, L. D.; Zhang, H.; Bradshaw, D. *J. Mater. Chem.* **2010**, *20*, 5720−5726.
(51) Lu, A.-H.; Li, W.-C.; Muratova, N.; Spliethoff, B.; Schüth, F. *Chem. Commun.* **2005**, 5184−5186.
(52) Li, Z. J.; Cul, G. D. D.; Yan, W. F.; Liang, C. D.; Dai, S. *J. Am. Chem. Soc.* **2004**, *126*, 12782−12783.
(53) Oh, J.-M.; Kumbhar, A. S.; Geiculescu, O.; Creager, S. E. *Langmuir* **2012**, *28*, 3259−3270.
(54) Li, Z. J.; Yan, W. F.; Dai, S. *Langmuir* **2005**, *21*, 11999−12006.
(55) Silvestre-Albero, J.; Wahby, A.; Sepúlveda-Escribano, A.; Martínez-Escandell, M.; Kanekob, K.; Rodríguez-Reinoso, F. *Chem. Commun.* **2011**, *47*, 6840−6842.
(56) Banerjee, R.; Furukawa, H.; Britt, D.; Knobler, C.; O'Keeffe, M.; Yaghi, O. M. *J. Am. Chem. Soc.* **2009**, *131*, 3875−3877.
(57) An, J.; Geib, S. J.; Rosi, N. L. *J. Am. Chem. Soc.* **2010**, *132*, 38−39.
(58) Wang, L. F.; Yang, R. T. *J. Phys. Chem. C* **2012**, *116*, 1099−1106.
(59) Ortiz, G.; Brandès, S.; Rousselin, Y.; Guilard, R. *Chem.—Eur. J.* **2011**, *17*, 6689−6695.